Check for updates

Structural and ferroelectric properties of perovskite Pb$_{(1-x)}$(K$_{0.5}$Sm$_{0.5}$)$_x$TiO$_3$ ceramics†

Arun Kumar Yadav,[a] Anita,[a] Sunil Kumar, [ID][a] Anjali Panchwanee,[c]
V. Raghavendra Reddy,[c] Parasharam M. Shirage, [ID][ab] Sajal Biring[d]
and Somaditya Sen [ID] *[ab]

PbTiO$_3$ has the highest tetragonal distortion ($c/a \sim 1.064$) and highest spontaneous polarization among perovskite titanates. But, it is hazardous and hence one needs to reduce Pb content by substituting or reducing Pb content for use in practical applications. Pb$_{(1-x)}$(K$_{0.5}$Sm$_{0.5}$)$_x$TiO$_3$ ($0 \leq x \leq 0.5$) perovskite powders were synthesized by sol–gel process, where Pb^{2+} was replaced by a combination of K$_{0.5}$$^{1+}Sm_{0.5}$$^{3+}$ (equivalent charge and comparable ionic radius) providing an excellent substitution model to study changes in structural and electrical properties. Vibrational properties and dielectric properties are modified with substitution. A polar *tetragonal* to a nearly nonpolar *cubic* phase transition decreases to lower temperatures with substitution due to the reduction of the lattice strain with substitution. Ferroelectricity is retained even for $x = 0.5$, which has a nearly *cubic* phase and makes the material technologically important.

1. Introduction

Properties like ferroelectricity, piezoelectricity, and pyroelectricity were discovered in perovskite ABO$_3$ compounds. Ferroelectrics are used in energy conversion devices, ultrasonic medical diagnostic apparatus, ultrasonic non-destructive detectors, pyroelectric infrared sensors and magnetoelectric sensors.[1–3] Pb-based ceramics are used in sensors, actuators, capacitors, nonvolatile memories, ultrasonic transducers, high piezoelectric, electromechanical and electro-optic properties *etc.*[4,5] PbTiO$_3$ has a structural phase transition from tetragonal (*P4mm*) to cubic (*Pm3m*) at 763 K. It has a highly strained lattice due to strong orbital hybridization and subsequent non-centrosymmetric lattice distortion. Among the perovskites, PbTiO$_3$ has the highest tetragonal distortion ($c/a \sim 1.064$) which makes it significantly more ferroelectric with the highest spontaneous polarization.[6,7] But, Pb not being an environmental friendly material due to highly toxic nature of Pb, there is a necessity to reduce the Pb content for applications from the point of view of safety and health concerns. Substituted PbTiO$_3$ compounds have been explored to investigate the science and

applicability of these materials. A few such ferroelectric ceramics materials are Pb(Mg$_{1/3}$Nb$_{2/3}$)O$_3$–xPbTiO$_3$, Ba(Mg$_{1/3}$Nb$_{2/3}$)O$_3$–xPbTiO$_3$, Ba(Zn$_{1/3}$Nb$_{2/3}$)O$_3$–xPbTiO$_3$, Ba(Yb$_{1/2}$Nb$_{1/2}$)O$_3$–xPbTiO$_3$, Ba(Sc$_{1/2}$Nb$_{1/2}$)O$_3$–xPbTiO$_3$, BaSnO$_3$–xPbTiO$_3$, $(1 - x)$-PbTiO$_3$–xBi(Zn$_{1/2}$Ti$_{1/2}$)O$_3$, $(1-x)$PbTiO$_3$–xBi(Ni$_{1/2}$Ti$_{1/2}$)O$_3$, Pb(In$_{1/2}$Nb$_{1/2}$)O$_3$–Pb(Mg$_{1/3}$Nb$_{2/3}$)O$_3$–PbTiO$_3$, PbHfO$_3$–Pb(Mg$_{1/3}$Nb$_{2/3}$)O$_3$–PbTiO$_3$, Pb(Sn, Ti)O$_3$–Pb(Mg$_{1/3}$Nb$_{2/3}$)O$_3$–xPbTiO$_3$, Pb(Ho$_{1/2}$Nb$_{1/2}$)O$_3$–Pb(Mg$_{1/3}$Nb$_{2/3}$)O$_3$–PbTiO$_3$, Pb(Y$_{1/2}$Nb$_{1/2}$)O$_3$–Pb(Mg$_{1/3}$Nb$_{2/3}$)O$_3$–PbTiO$_3$ and $(1 - x)$PbTiO$_3$–xBiFeO$_3$ *etc.*[8–19] By making isovalent or aliovalent substitution on the Pb^{2+} site, lattice anisotropy is reduced. A polar *tetragonal* to nonpolar *cubic* phase transition decreases to lower temperatures mostly decreases with substitution as most substitution reduces the lattice strain. Also the phase transition is diffused due to cumulative structural transition resulting from the different T_C for a localized region in given system, resulting in a broad peak with temperature in dielectric response rather than sharp peak in normal ferroelectrics.[20–22]

A combination of K$_{0.5}$$^{1+}Sm_{0.5}$$^{3+}$ provides the same charge and a comparable ionic radius as compared to Pb^{2+}. Thus this combination may provide an excellent substitution model enabling a detailed study of changes in the physical properties. In this study we report for the first time a new series, Pb$_{(1-x)}$-(K$_{0.5}$Sm$_{0.5}$)$_x$TiO$_3$ ($0 \leq x \leq 0.50$). Detailed studies of the structure, vibrational, dielectric and ferroelectric properties are analyzed.

2. Materials and methods

Sol–gel processed polycrystalline Pb$_{(1-x)}$(K$_{0.5}$Sm$_{0.5}$)$_x$TiO$_3$ ($0 \leq x \leq 0.5$) (PKST) ceramics were prepared using hydrated Lead(II)

[a]Discipline of Metallurgy Engineering and Materials Science, Indian Institute of Technology, Khandwa Road, Indore-453552, India. E-mail: sens@iiti.ac.in

[b]Discipline of Physics, Indian Institute of Technology, Khandwa Road, Indore-453552, India

[c]UGC-DAE Consortium for Scientific Research, University Campus, Khandwa Road, Indore-452001, India

[d]Electronic Engg., Ming Chi University of Technology, New Taipei City, Taiwan

† Electronic supplementary information (ESI) available. See DOI: 10.1039/c7ra07130b

nitrate ($Pb(NO_3)_2$), Potassium nitrate (KNO_3), Samarium oxide and Titanium(IV) bis(ammonium lactato) dihydroxide (TALH) solution as precursors with purity > 99.999% (Alfa Aesar, Puratronic grade). Sm_2O_3 was dissolved in dilute HNO_3. TALH, $Pb(NO_3)_2$ and KNO_3 were dissolved in double distilled water. Sm and Ti solutions were mixed together and thereafter the K solution was added to form a mixed solution of Sm, Ti and K and stirred for a while. The Pb solution was added to this combined solution. A solution of citric acid and ethylene glycol of 1 : 1 molar ratio was prepared in a separate beaker as gel former and was thereafter added to the mixture. Appropriate amount of ammonium hydroxide was added to the solution to maintain a pH = 8.5. The resultant sols were vigorously stirred and heated at ~85 °C on a hot plate to form gels. The gels were burnt to form black powders. To de-carbonate and de-nitrate, these powders were heated at 500 °C for 12 h.

Pellets (diameter ~ 10 mm; thickness ~ 1.5 mm) were prepared by uni-axially pressing the carefully grinded powders mixed with a binder PVA solution. The pellets were sintered at 600 °C for 6 h to burn the binder followed by another heating at 1050 °C for 6 h to form mechanically dense pellets. Densities of the samples were estimated from the weights and dimensions of the pellets. The theoretical densities were also estimated using formula weight and volume of unit cells calculated from the refined lattice parameters of the samples. Relative densities range from ~93%, 94%, 95%, 95%, 95%, 92%, and 91% for compositions with $x = 0.06$, 0.09, 0.12, 0.18, 0.25, 0.37, and 0.50, respectively.

X-ray diffraction (XRD) was performed using Bruker D2 Phaser X-ray Diffractometer to ensure the phase formation and purity of the sintered samples. Raman spectroscopy was performed using a Czerny–Turner type achromatic spectrograph with spectral resolution of 0.4 cm^{-1}/pixel and excitation of 632.8 nm. Microstructure and the grain size analysis of the sintered pellets were investigated by Supra55 Zeiss field emission scanning electron microscope. Electrodes were prepared using silver paste painted on both sides of the sintered pellet. Silver coated pellets were cured at 550 °C for 10 minutes. Before doing the measurement, we heated the samples at 200 °C for 10 minutes to avoid any moisture content.

A Newtons 4th LTD PSM 1735 LCR meter was used to study the dielectric properties. Ferroelectric (P–E) studies were carried out by ferroelectric loop (P–E) tracer (M/s Radiant Instruments, USA). During the ferroelectric measurements, the samples were immersed in silicone oil to prevent electric arcing, at high applied voltages.

3. Results and discussion

3.1 Structural properties

X-ray powder diffraction (XRD) patterns of the PKST powders with $0 \leq x \leq 0.5$, were analyzed after crushing the pellets sintered at 1050 °C. The XRD patterns are shown in Fig. 1a. With increasing substitution, the separation between the (001) and (100) peaks reduces. All the compositions belong to a tetragonal space group $P4mm$ phase. A very weak XRD peak (indicated with star symbol) belonging to the $PbTiO_3$ related compound

$Pb_2Ti_2O_6$ which has same composition as of $PbTiO_3$ but crystal structure is a pyrochlore ($A_2B_2O_7$-type) with one vacant oxygen site[23] [Fig. 1a]. A Le Bail profile fitting of the XRD data was done with Topas3.2 software to estimate the lattice parameters. The goodness of the fitting for $x = 0.06$ is shown in Fig. 1d. Lattice parameter 'c' decreases with increasing composition x, while 'a' is almost constant (Fig. 1b). Hence the c/a ratio decreases to ~1 for $x = 0.5$ (Fig. 1c). The variation of lattice parameters with composition is also a signature of proper substitution of Pb by K/Sm.

In perovskite ABO_3 samples, tolerance factor is a quantitative measure of the mismatch between the bonding requirements of A and B-site cations and subsequently reflects structural distortions such as rotation/tilt of the B-octahedral. Lattice stability and distortion of crystal structures are related to this mismatch[24] and hence can be estimated from the tolerance factor (t), given by,

$$t = \frac{(R_A + R_O)}{\sqrt{2}(R_B + R_O)} \tag{1}$$

where, R_A, R_B and R_O are the radii of A and B-site ions and O ions, respectively. Since the average A-site ionic radii of the substituent are lesser compared to Pb, tilt as well as non-centrosymmetric distortion will reduce. The merging peaks in the XRD data indicate a transformation from non-centrosymmetric to centrosymmetric structure.[25,26] The tolerance factor of the PKST samples decreases from 1.019 as in $x = 0$ to 0.988 for $x = 0.5$, also the strain decreases with increasing substitution.

Room temperature Raman spectroscopy [Fig. 2] was done to qualitatively assess retention of domain structure, defects and structural distortions and thereby understand deformations and lattice strains associated with substitution in PKST. All the observed modes belong to pure $PbTiO_3$ having tetragonal space group symmetry (C_{4v}^1) with 12 optical modes attributed to three A_1-symmetry modes, eight E-symmetry modes (four degenerate pairs) and a B_1-symmetry mode.[27–29]

Intensity of the A_1(1TO), A_1(2TO) and A_1(3TO) reduces with increasing substitution. Among the A_1 modes the most intense mode is A_1(1TO). This mode merges with the E(1TO) mode to form the T_{1u} mode in the cubic form. The A_1(1TO) mode is due to oscillations of the Ti-octahedra (i.e. Ti and O together) relative to Pb ions.[30] This mode does not soften much but nearly vanishes after $x = 0.09$ and reappears again for $0.25 \leq x \leq 0.5$. The A_1(2TO) mode is due to oscillations of the Ti ion relative to O and Pb ions. This mode softens nominally until $x = 0.09$ but thereafter drastically softens to merge with the E(2TO) mode in $x = 0.5$. A similar but less drastic trend is observed for the A_1(3TO) mode, in which the Ti ions and the apical O ions together form a chain and vibrates along the c-axis with respect to the Pb and the other O atoms. From all these three modes it is understood that relative motion between the Pb, Ti and O ions reduces along the c-axis with substitution. In Fig. 2, we have shown a pictorial representation of all the vibrational modes of $PbTiO_3$. The corner gray ions represent Pb while the central blue ones represent Ti ions. The smaller green spheres represent
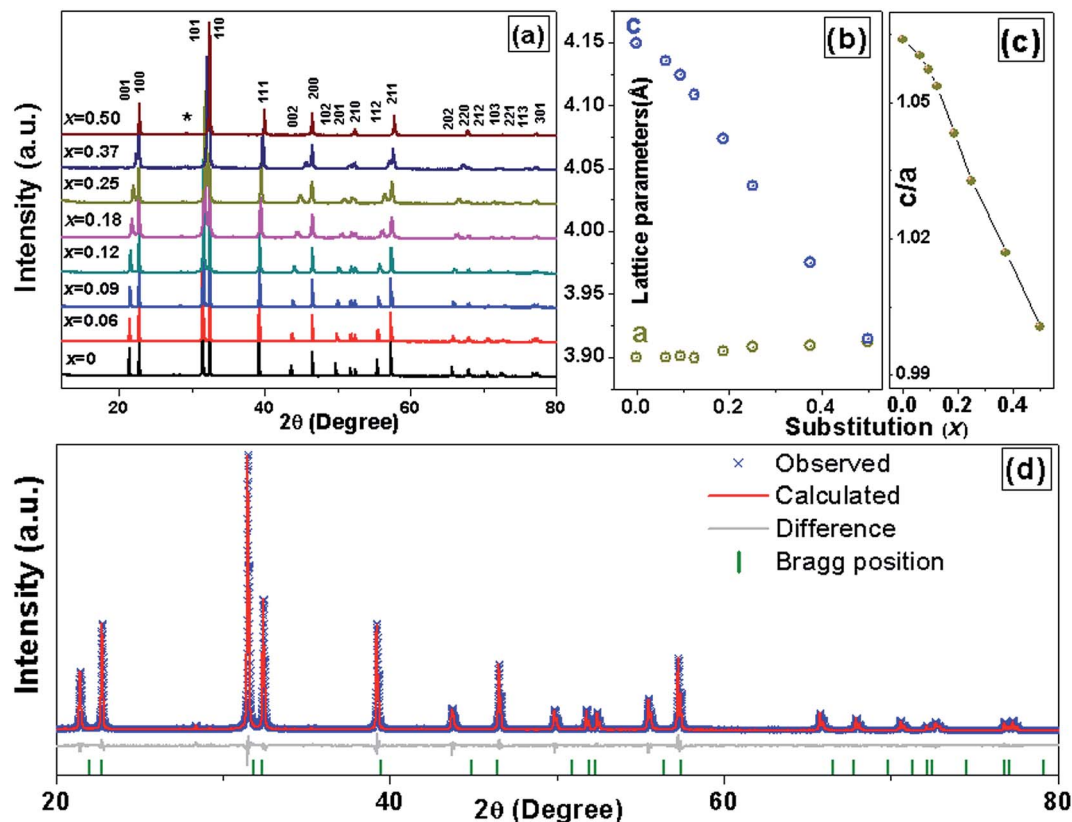
Fig. 1 (a) X-ray powder diffraction patterns of $Pb_{(1-x)}(K_{0.5}Sm_{0.5})_xTiO_3$ samples, (b) lattice parameters, (c) tetragonal strain, c/a ratio at room temperature. (d) LeBail profile fitting of $Pb_{(1-x)}(K_{0.5}Sm_{0.5})_xTiO_3$ for $x = 0.06$ composition where the crosses are observed data points, the solid line is calculated data and line below is the difference between observed and calculated data. The vertical bars are the Bragg position of the reflection in the $P4mm$ space group.

oxygen ions. All the ions lie on the x–y basal plane. The plus sign represents ions vibrating out of the plane of paper while minus represents the opposite direction. The directions of the in-plane vibrations are shown by the arrows.

The tetragonal $PbTiO_3$ is a strained lattice. The strain originates from a very strong hybridization between $Pb(6s^2)$–$O(2p)$ and also due to a moderate $Ti(3d)$–$O(2p)$ hybridization.[2,31] As a result of substitution of Pb by K/Sm, we expect a reduction of
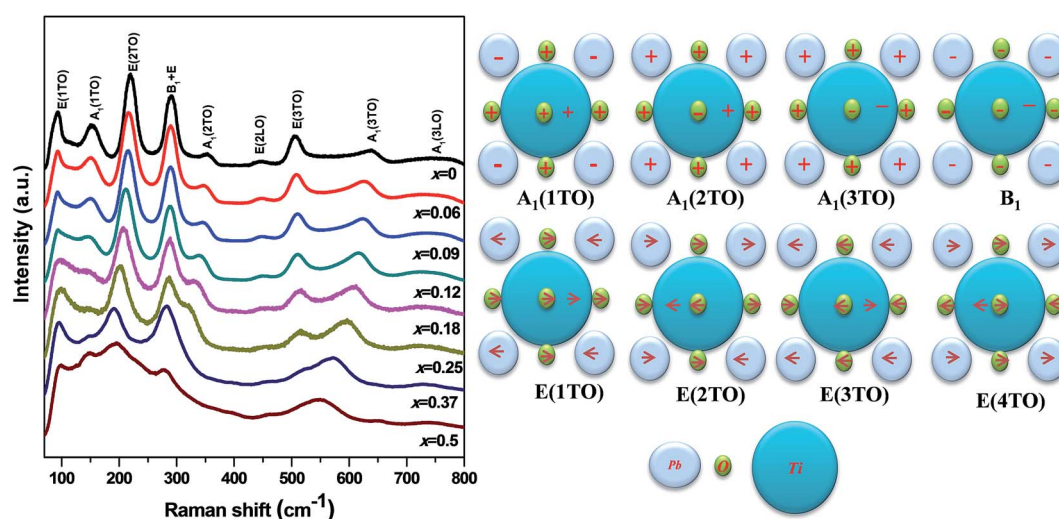

Fig. 2 (Left) Raman spectra of $Pb_{(1-x)}(K_{0.5}Sm_{0.5})_xTiO_3$ samples at room temperature. (Right) Cartoon shows different modes and their related vibration type.[27]

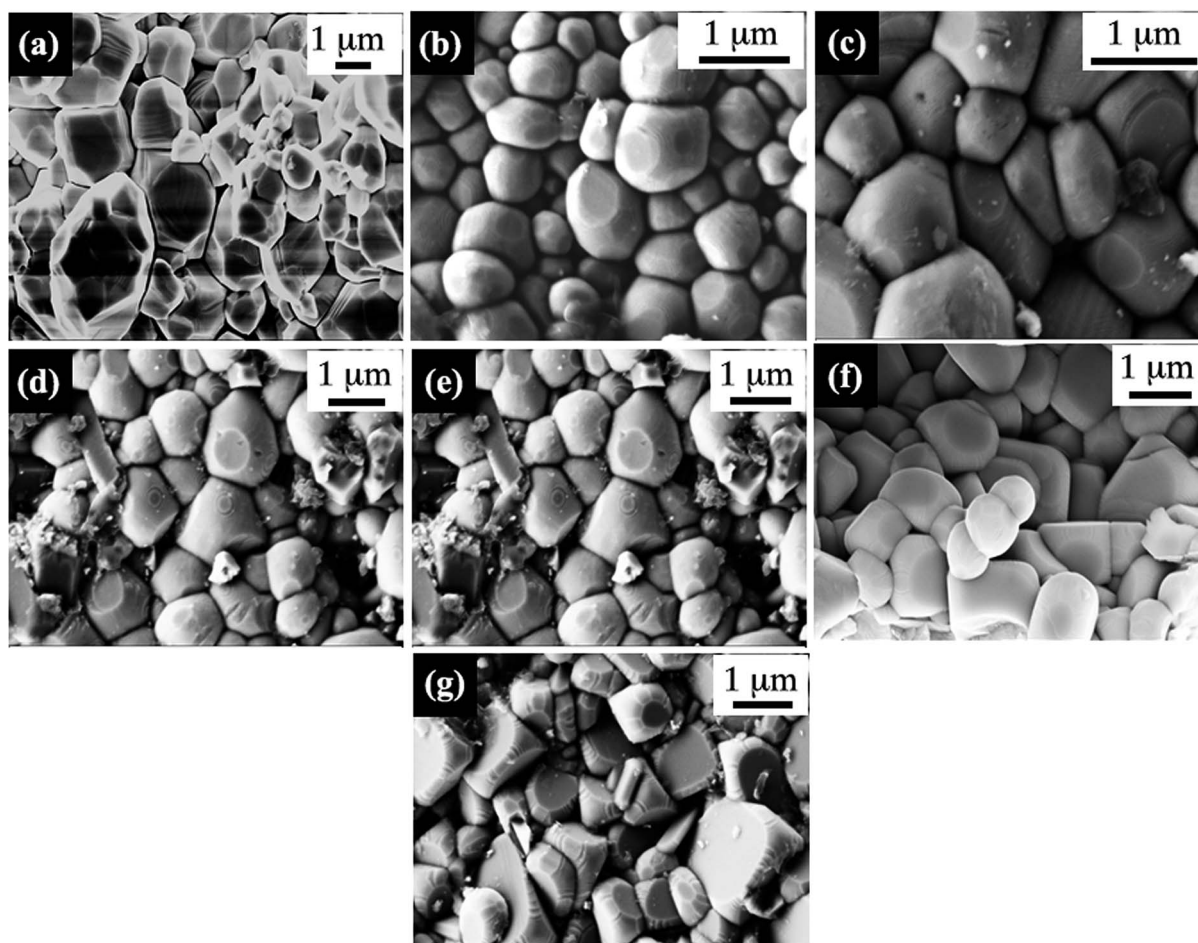**Fig. 3** Microstructure analysis of $Pb_{(1-x)}(K_{0.5}Sm_{0.5})_xTiO_3$ samples, (a) $x = 0.06$, (b) $x = 0.09$, (c) $x = 0.12$, (d) $x = 0.18$, (e) $x = 0.25$, (f) $x = 0.37$, and (g) $x = 0.50$ compositions.

the strong $Pb(6s^2)$–$O(2p)$ bond. This reduction in the strength of the bond reduces energy of vibration which is reflected in the softening of the $A_1(2TO)$. Such a reduction in energy in the $A_1(1TO)$ mode is not observed as in this mode, the A-site is freely oscillating with respect to the Ti–O octahedron. However the lesser number of oscillators reduce the intensity of $A_1(1TO)$ and $A_1(2TO)$. Note that the $E(3TO)$ mode gains energy with the substitution. The lower mass of K/Sm compared to Pb may be a reason for the same.

The most noticeable significance of the Raman measurement is that even at $x = 0.50$ we observe all the modes where from XRD $c/a \sim 1$. Such an observation hints at the fact that a remnant strain which may or may not be related to the tetragonal structure is retained in the high x samples. In the cubic mode, pure $PbTiO_3$ does not have any Raman mode, as all the $A_1(TO)$ and $E(TO)$ modes merge and vanish gradually at the phase transition.[27]

FESEM images of PKST ceramic samples are recorded in $0.06 \leq x \leq 0.50$ range (Fig. 3). Grains are closely packed in all the samples. The average grain size calculated from the FESEM is 1.19 ± 0.53 μm for the composition with $x = 0.06$ which decreases to 0.98 ± 0.37 μm for $x = 0.50$. The average grain size

seams to decrease nominally with increasing K/Sm substitution. This behavior could be attributed to lower diffusivity of rare earth during sintering. Similar behavior has been observed in other rare earth doped perovskites and layered perovskites.[32,33]

3.2 Dielectric properties

Room temperature (RT) dielectric properties were measured as a function of frequency for PKST ($0.06 \leq x \leq 0.50$). As shown in Fig. 4a and 1S,† with increasing frequency the value of dielectric constant (ε') and loss (tan δ) decrease at low frequency range (100 Hz to 10 kHz) and remains almost constant in high frequency region. Space charge polarization may contribute to higher values of dielectric constant. We observe that with increasing substitution, the value of ε' of PKST ceramics increases exponentially [Fig. 4b]. This behavior of ε' at room temperature and similar trend in tan δ can be attributed to the higher dipolar polarizability of K/Sm than Pb.[34,35] For $x = 0.50$, ε' increases rapidly probably due to its near room temperature phase transition.

To study the phase transition in PKST and other dielectric properties, capacitance and dielectric loss factor were measured over the temperature range of 300–773 K at various frequencies

in 1 kHz to 1 MHz range. It was quite difficult to fabricate a pure phase, sufficiently dense and mechanically robust $PbTiO_3$ pellet. Hence, dielectric properties of $PbTiO_3$ phase were not investigated.

Pure $PbTiO_3$ undergoes a sharp ferroelectric to paraelectric transition accompanied by a structural transition from polar tetragonal to non-polar cubic phase.[36] In such ferroelectrics, we observe maxima in the ε'–T data, associated with this phase transition. For $PbTiO_3$ the reported phase transition temperature is around 763 K (Curie temperature). In the PKST samples this phase transition temperature (T_m) varies from 680 K for $x = 0.06$ to 341 K as in $x = 0.50$. Note that the transition temperature is not frequency dependent; thereby the samples are not relaxors.

The phase transition temperature approximately decreases linearly with substitution [Fig. 4c]. The Pb $6s^2$ lone pair helps in stabilizing the tetragonal strain ($\sim$6%) in $PbTiO_3$.[37] We have shown from our XRD and Raman analysis that with increasing substitutions the tetragonal strain is relieved in PKST. The reduction of tetragonal distortion reduces with substitution thereby requiring lesser thermal energy to achieve centrosymmetric cubic structure. Therefore with increasing x, phase transition temperature decreases. Similar trend has been observed in other perovskite related ferroelectrics.[38]

Another feature in [Fig. 4d to j] is an apparent increase in diffuseness of peak in ε'–T plots. Diffuse phase transition is usually observed in perovskites with random distribution of different types of ions on structurally identical sites in lattice. It must be noted that diffuse phase transition exhibit a broad change of structure and properties at the Curie point compared to a sharp peak in normal ferroelectric materials;[39–41] consequently, the phase transition characteristics of such materials are known to diverge from the characteristic of Curie–Weiss behavior and can be described by a modified Curie–Weiss formula.[42,43]

$$\frac{1}{\varepsilon'} - \frac{1}{\varepsilon'_m} = C^{-1}(T - T_m)^\gamma \qquad (2)$$

where, C is Curie–Weiss constant and γ ($1 \leq \gamma \leq 2$) gives the degree of diffuseness. A value of $\gamma = 2$ describes an ideal diffuse phase transition. The degree of diffuseness was calculated by the least-square linear fitting of $\ln\left(\frac{1}{\varepsilon'} - \frac{1}{\varepsilon'_m}\right)$ *versus* $\ln(T - T_m)$ curves at a frequency of 1 MHz of PKST ceramics. The slope of linear fit, was found to increase from 1.136 ± 0.007 for $x = 0.06$ to 1.693 ± 0.019 for $x = 0.50$ indicating a significant increase in diffuseness of phase transition in doped samples (Fig. 4c). Compositional disorder arising due to the random distribution of K^+ and Sm^{3+} seems to be responsible for observed diffuse phase transition in PKST ceramics.
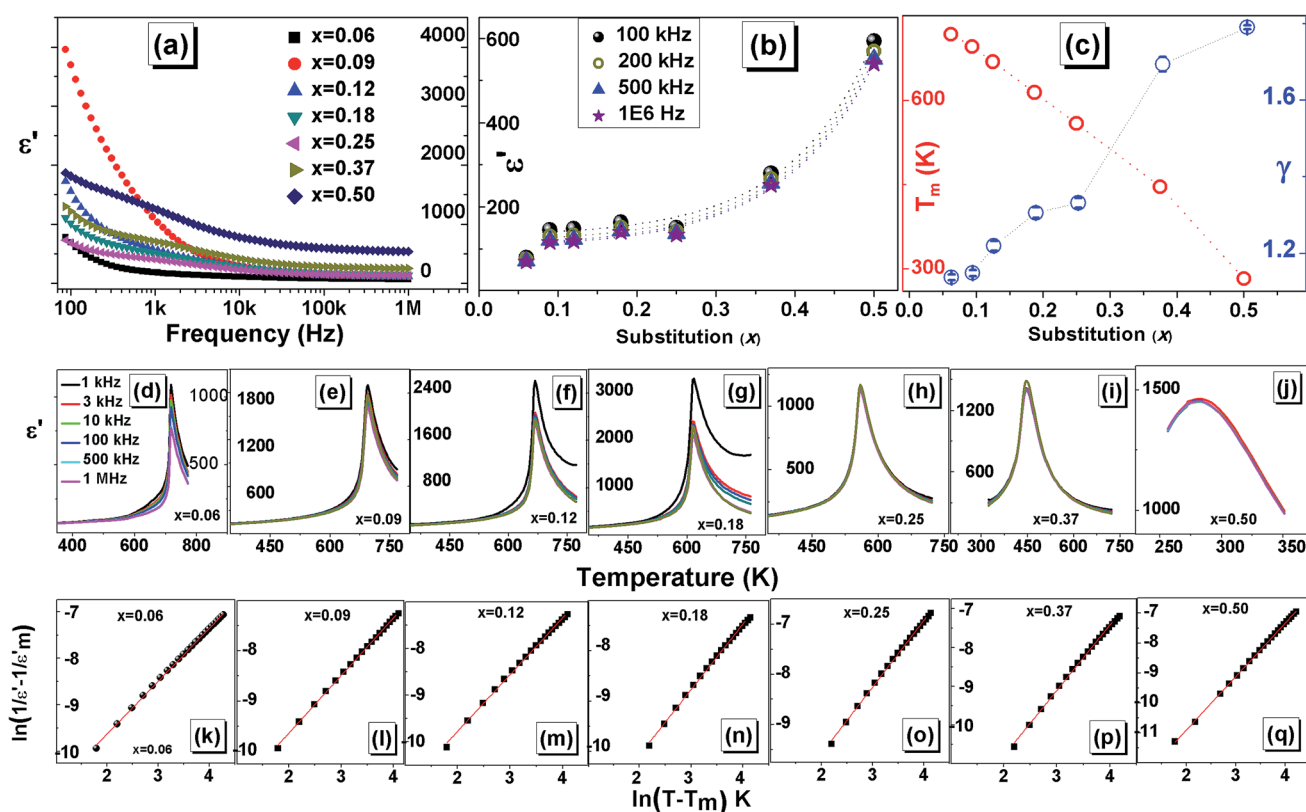

Fig. 4 (a) Frequency dependence of dielectric constant of $Pb_{(1-x)}(K_{0.5}Sm_{0.5})_xTiO_3$, (b) composition dependence of high frequency dielectric constant at room temperature; (c) phase transition temperature (T_m) and degree of diffusivity (γ) with composition x; (d–j) permittivity data for high frequency as a function of temperature for PKST samples; (k–q) linear fitting of $\ln[(1/\varepsilon') - (1/\varepsilon'_m)]$ *versus* $\ln(T - T_m)$ (modified Curie–Weiss law) at 1 MHz, solid lines representing the fitted data.

Impedance spectroscopy enables to determine the various contributions to dielectric constant, such as grain, grain boundaries and electrode effect.[44] Impedance of such type of system can be described by the Cole–Cole equation[45]

$$Z^*(\omega) = \frac{R_1}{1 + (j\omega\tau)^{1-\alpha}} \qquad (3)$$

The real (Z') and imaginary (Z'') parts of impedance can be written in the following manner:

$$Z'(\omega) = \frac{R_1\left[1 + (\omega\tau)^{1-\alpha}\sin\left(\frac{\alpha\pi}{2}\right)\right]}{1 + 2(\omega\tau)^{1-\alpha}\sin\left(\frac{\alpha\pi}{2}\right) + (\omega\tau)^{2-2\alpha}} \qquad (4)$$

$$Z''(\omega) = \frac{R_1(\omega\tau)^{1-\alpha}\cos\left(\frac{\alpha\pi}{2}\right)}{1 + 2(\omega\tau)^{1-\alpha}\sin\left(\frac{\alpha\pi}{2}\right) + (\omega\tau)^{2-2\alpha}} \qquad (5)$$

with Cole–Cole parameter, $\alpha = 2\theta/\pi$ being a measure of distribution of relaxation time, $\tau = R_1 C$, related to the resistance R_1 and capacitance C associated with grain.

The imaginary, Z'' (capacitive) and the real, Z' (resistive) impedances are plotted in Fig. 5. Capacitance due to grain boundary contribution is generally much higher than that of grain.[44] This may be due to grains having less resistance than grain boundary. In the Nyquist plot these effects are generally observed as three semicircles; the first smaller one belonging to grain, second grain boundary followed by the electrode contribution. Our results show only one semicircle. This contribution seems to be from the grain as the semicircle starts from origin (high frequency regime) and at high frequency we have observed a steady dielectric constant. Note that, it may possible

due to less resistance at grain boundary, its effect suppresses and merge with grain effect. Also note that the resistance of the sample has increased with substitution Fig. 5 (right hand side). The increasing resistance is an indication of better charge retention properties, enhancing the capability of being a polarizable material. Time constant or relaxation time (τ) is multiplication of resistant and capacitance. Accordingly, increase in resistance and capacitance increases the time constant with increase in x. In addition, increase in temperature decreases the relaxation time for all compositions.

3.3 Ferroelectric properties

For $0.06 \leq x \leq 0.37$ the structure is elongated tetragonal type and a strained lattice is expected result in spontaneous polarization. It is to be noted that the tetragonality decreases with substitution until $x = 0.5$ where the phase is cubic-like. This hints at reducing ferroelectricity with substitution. Also, the Raman modes broaden with increasing x hinting at dispersed vibrational motion of the phonons. The $A_1(1TO)$ mode is related to the vibration and distortion of the Ti–O bonds and thereby to ferroelectricity. The mode sustains for all samples although getting diminished with substitution. The dielectric properties show shifting of phase transition towards lower temperatures with increasing x, suggesting existence of ferroelectricity at room temperature.

The electric field dependent polarization (P–E hysteresis) and instantaneous current (I–E hysteresis) at 1 Hz frequency have been reported for all the compositions. For $0.06 \leq x \leq 0.12$, P–E hysteresis loops [Fig. 6] appears to be lossy dielectric type[46,47] rather than typical ferroelectric. Also, no signature of domain switching is observed in I–E data for $x \leq 0.12$ (Fig. 6). The leaky, lossy nature may be due to comparatively lower resistances of the lesser modified samples (observed from impedance studies). For $x > 0.12$, the leaky nature decreases and
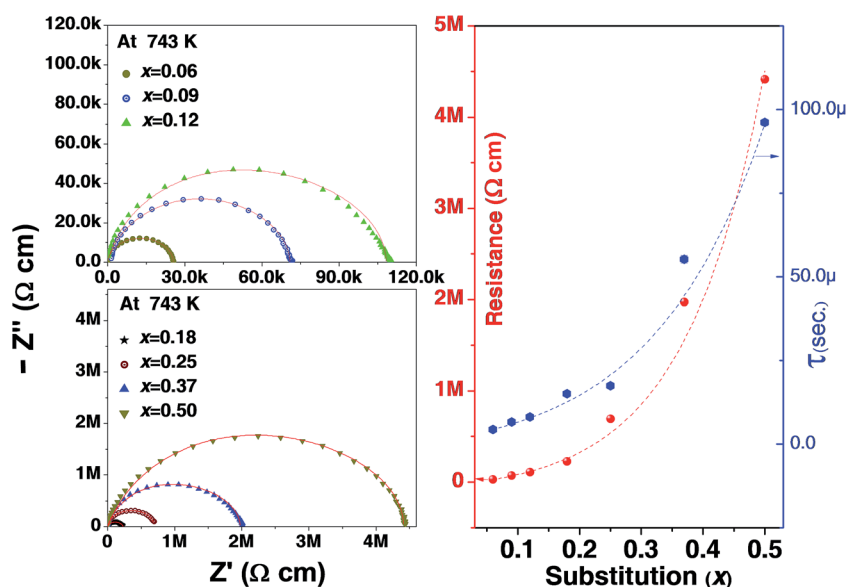

Fig. 5 (Left) Nyquist plots of $Pb_{(1-x)}(K_{0.5}Sm_{0.5})_xTiO_3$ samples at 743 K, (Right) resistance and time constant (τ), extracted from fitting of Nyquist-plots by Cole–Cole equation for all the samples.
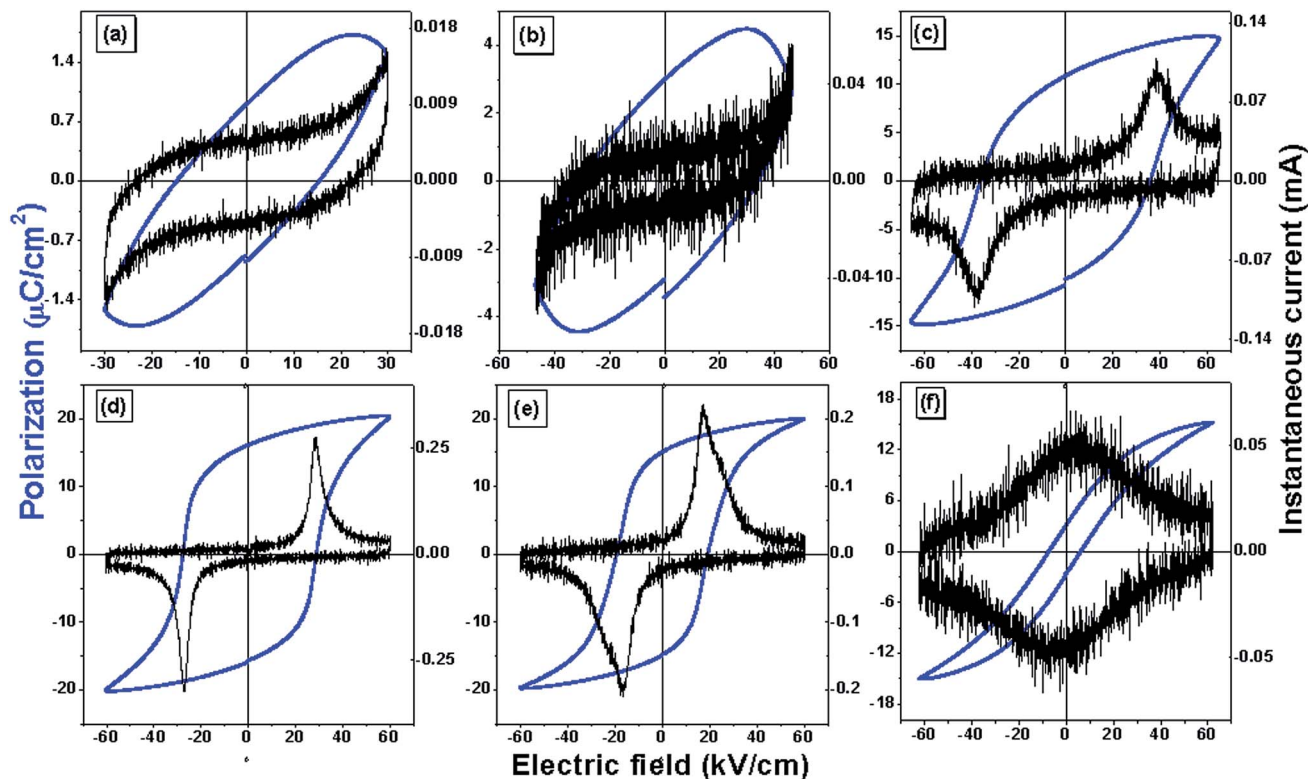
Fig. 6 Polarization and instantaneous current *versus* electric field of $Pb_{(1-x)}(K_{0.5}Sm_{0.5})_xTiO_3$ samples, (a) $x = 0.06$ (b) $x = 0.12$ (c) $x = 0.18$ (d) $x = 0.25$ (e) $x = 0.37$ (f) $x = 0.50$.

proper hysteresis *P–E* loops were observed. For $x = 0.5$, it is expected a non-ferroelectric sample due to its cubic-like structure. However, we find a slim *P–E* loop with a weak *I–E* data. This hints at a nearly cubic structure for $x = 0.5$. A detailed structural work needs to be done on this sample which is beyond the scope of this study. For a maximum applied field of 60 kV cm^{-1} the sample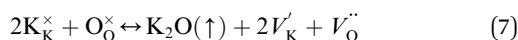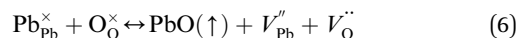 with $x = 0.25$ shows highest apparent remnant polarization of 15.9 μC cm^{-2} and a coercive field of 27.2 kV cm^{-1}. These values reduce with substitution to 2.97 μC cm^{-2} and 6.91 kV cm^{-1} in $x = 0.5$ composition. A comparison of ferroelectric properties and phase transition temperature for a few PbTiO$_3$-based compositions with the compound $Pb_{0.750}Na_{0.125}Sm_{0.125}TiO_3$ (studied in the present investigation) is provided in Table 1.

Table 1 Remnant polarization, coercive field, and phase transition temperature for few selected PbTiO$_3$-based compounds

Composition	Remnant polarization (P_r)	Coercive field (E_c)	Applied electric field at room temperature	T_c (phase transition temperature)
PbTiO$_3$ single crystal (001) oriented[48]	~57 μC cm^{-2}	—	± 20 kV cm^{-1}	~490 °C
Pb(Ho$_{1/2}$Nb$_{1/2}$)O$_3$–Pb(Mg$_{1/3}$Nb$_{2/3}$)O$_3$–PbTiO$_3$ single crystal (001) oriented[18]	~24.5 μC cm^{-2}	~3.22 kV cm^{-1}	±7.5 kV cm^{-1}	~140 °C
Pb(Mg$_{1/3}$Nb$_{2/3}$)O$_3$–PbTiO$_3$ (011)-oriented single crystal[49]	~28.9 μC cm^{-2}	~1.2 kV cm^{-1}	±8 kV cm^{-1}	—
PLT8 thin film (Pb$_{1-x}$La$_x$Ti$_{1-x/4}$O$_3$ for $x = 0.08$)[50]	~18.5 μC cm^{-2}	~144 kV cm^{-1}	—	~330 °C
Pb(Zr$_{0.532}$Ti$_{0.468}$)O$_3$ ceramics[51]	~26.2 μC cm^{-2}	~18.4 kV cm^{-1}	—	~359 °C
Pb$_{1-x}$La$_x$(Zr$_{0.52}$Ti$_{0.48}$)O$_3$ for $x = 0.05$ ceramic[52]	8.99 μC cm^{-2}	6 kV cm^{-1}	—	~105 °C
Pb$_{1-x}$(K$_{0.5}$Sm$_{0.5}$)$_x$TiO$_3$ for $x = 0.25$ ceramic	15.9 μC cm^{-2}	27.2 μC cm^{-2}	±60 kV cm^{-1}	~286 °C

Improvement of ferroelectric properties at room temperature in PKST samples results from increase of resistive and capacitive properties. In $PbTiO_3$, Pb and O vacancies are a common feature and results in non-stoichiometric samples mostly originating due to high volatility of Pb and subsequent O-vacancies due to missing Pb ions. By K/Sm substitution, Pb content is less, thereby evaporation of volatile matter is reduced. Therefore, Pb vacancies and resultant oxygen vacancies are reduced resulting in more stoichiometric samples. Although K is also volatile, the charge of the K ion is lesser than the Pb ion and hence O vacancies will be lesser. Vacancies play a very important role and enhance the conductivity of materials.[53–55] The defect structure can be represented by the Kröger–Vink notation:[56]

$$Pb_{Pb}^{\times} + O_{O}^{\times} \leftrightarrow PbO(\uparrow) + V_{Pb}'' + V_{O}^{\cdot\cdot} \qquad (6)$$

$$2K_{K}^{\times} + O_{O}^{\times} \leftrightarrow K_2O(\uparrow) + 2V_{K}' + V_{O}^{\cdot\cdot} \qquad (7)$$

Oxygen vacancies in perovskites can contribute to transport by migration from one site to another along the direction of applied high electric field increasing mobility and accumulate in the places with low free energy, such as domain walls and interfaces with electrodes. Accumulation of these oxygen vacancies at the domain boundary causes domain pinning. This restricts polarization switching.[57]

4. Conclusion

$(K_{0.5}Sm_{0.5})$ substituted $PbTiO_3$ ceramic samples were synthesized by sol–gel process. X-ray diffraction confirmed a tetragonal $P4mm$ phase. Lattice parameter 'c' decreases with increasing composition x, while 'a' is almost constant. Raman spectroscopy shows changes in intensity and energy of phonon modes related to tetragonal-cubic phase transformations and lattice strain with ferroelectric property. The lower mass of K/Sm compared to Pb may be a reason for such changes. However, in spite of the tetragonal-near cubic transformation the existence of Raman modes even for $x = 0.50$ hints at the fact that either some local tetragonality is retained or some other phenomenon apart from a tetragonal structure generates strain which can be attributed to the remnant polarization for $x = 0.5$ sample. High temperature dielectric study clearly indicates a dielectric phase transition which moves towards lower temperature with increasing substitution. The diffuseness of the phase transition increases with substitution due to compositional disorder arising due to the random distribution of K^+/Sm^{3+}. As a result we find changes in ferroelectric property which is for lower substitutions not much of significance due to the leaky nature but with increasing resistance becomes more effective and promising as a ferroelectric. However the remnant polarization decreases with substitution probably due to reduction in tetragonality.

Conflicts of interest

There are no conflicts to declare.

Acknowledgements

References

1 H. S. Bhatti, S. T. Hussain, F. A. Khan and S. Hussain, *Appl. Surf. Sci.*, 2016, **367**, 291–306.

2 H. Zhao, J. Miao, L. Zhang, Y. Rong, J. Chen, J. Deng, R. Yu, J. Cao, H. Wang and X. Xing, *Dalton Trans.*, 2016, **45**, 1554–1559.

3 T. F. Zhang, X. G. Tang, Q. X. Liu, Y. P. Jiang, X. X. Huang and Q. F. Zhou, *J. Phys. D: Appl. Phys.*, 2016, **49**, 095302.

4 E. C. Paris, M. F. C. Gurgel, M. R. Joya, G. P. Casali, C. O. Paiva-Santos, T. M. Boschi, P. S. Pizani, J. A. Varela and E. Longo, *J. Phys. Chem. Solids*, 2010, **71**, 12–17.

5 G. Sághi-Szabó, R. E. Cohen and H. Krakauer, *Phys. Rev. Lett.*, 1998, **80**, 4321–4324.

6 N. Jaouen, A. C. Dhaussy, J. P. Itié, A. Rogalev, S. Marinel and Y. Joly, *Phys. Rev. B: Condens. Matter Mater. Phys.*, 2007, **75**, 224115.

7 M. Adamiec, E. Talik and K. Wójcik, *J. Alloys Compd.*, 2007, **442**, 222–224.

8 Q. Wei and J. Cong, *Integr. Ferroelectr.*, 2015, **167**, 35–40.

9 D. D. Shah, P. K. Mehta, M. S. Desai and C. J. Panchal, *J. Alloys Compd.*, 2011, **509**, 1800–1808.

10 J. S. Forrester, J. S. Zobec, D. Phelan and E. H. Kisi, *J. Solid State Chem.*, 2004, **177**, 3553–3559.

11 I. Tomeno, J. A. Fernandez-Baca, K. J. Marty, K. Oka and Y. Tsunoda, *Phys. Rev. B: Condens. Matter Mater. Phys.*, 2012, **86**, 134306.

12 J. Chen, H. Shi, G. Liu, J. Cheng and S. Dong, *J. Alloys Compd.*, 2012, **537**, 280–285.

13 M. Algueró, P. Ramos, R. Jiménez, H. Amorín, E. Vila and A. Castro, *Acta Mater.*, 2012, **60**, 1174–1183.

14 D. Wang, M. Cao and S. Zhang, *J. Eur. Ceram. Soc.*, 2012, **32**, 433–439.

15 D. Wang, M. Cao and S. Zhang, *Phys. Status Solidi RRL*, 2012, **6**, 135–137.

16 D. Wang, M. Cao and S. Zhang, *J. Eur. Ceram. Soc.*, 2012, **32**, 441–448.

17 X. Li, Z. Wang, C. He, Y. Liu, X. Long, S. Han and S. Pan, *Mater. Lett.*, 2015, **143**, 88–90.

18 X. Li, Z. Wang, Y. Liu, C. He and X. Long, *CrystEngComm*, 2014, **16**, 7552–7557.

19 A. K. Yadav, V. Anita, S. Kumar, V. R. Reddy, P. M. Shirage, S. Biring and S. Sen, *J. Mater. Sci.: Mater. Electron.*, 2017, **28**, 10730–10738.

20 Y. Jia, H. Luo, S. W. Or, Y. Wang and H. L. W. Chan, *J. Appl. Phys.*, 2009, **105**, 124109.

21 X. P. Jiang, J. W. Fang, H. R. Zeng, B. J. Chu, G. R. Li, D. R. Chen and Q. R. Yin, *Mater. Lett.*, 2000, **44**, 219–222.

22 R. N. P. Choudhary and J. Mal, *Mater. Sci. Eng., B*, 2002, **90**, 1–6.

23 G. Xu, W. He, Y. Zhao, Y. Liu, Z. Ren, G. Shen and G. Han, *CrystEngComm*, 2011, **13**, 1498–1503.

24 D. I. Woodward and I. M. Reaney, *Acta Crystallogr., Sect. B: Struct. Sci.*, 2005, **61**, 387–399.

25 I. Grinberg, M. R. Suchomel, P. K. Davies and A. M. Rappe, *J. Appl. Phys.*, 2005, **98**, 094111.

26 N. Raengthon, C. McCue and D. P. Cann, *J. Adv. Dielectr.*, 2006, **06**, 1650002.

27 J. D. Freire and R. S. Katiyar, *Phys. Rev. B: Condens. Matter Mater. Phys.*, 1988, **37**, 2074–2085.

28 J. Frantti, V. Lantto, S. Nishio and M. Kakihana, *Phys. Rev. B: Condens. Matter Mater. Phys.*, 1999, **59**, 12–15.

29 G. Burns and B. A. Scott, *Phys. Rev. Lett.*, 1970, **25**, 167–170.

30 C. Sun, J. Wang, P. Hu, M. J. Kim and X. Xing, *Dalton Trans.*, 2010, **39**, 5183–5186.

31 V. R. Mastelaro, P. P. Neves, S. R. d. Lazaro, E. Longo, A. Michalowicz and J. A. Eiras, *J. Appl. Phys.*, 2006, **99**, 044104.

32 X. Chou, J. Zhai, H. Jiang and X. Yao, *J. Appl. Phys.*, 2007, **102**, 084106.

33 K. Sunil and K. B. R. Varma, *J. Phys. D: Appl. Phys.*, 2009, **42**, 075405.

34 J. Cheng, S. Yu, J. Chen, Z. Meng and L. E. Cross, *Appl. Phys. Lett.*, 2006, **89**, 122911.

35 http://ctcp.massey.ac.nz/Tablepol2014.pdf.

36 A. Sani, M. Hanfland and D. Levy, *J. Solid State Chem.*, 2002, **167**, 446–452.

37 H. Sharma, J. Kreisel and P. Ghosez, *Phys. Rev. B: Condens. Matter Mater. Phys.*, 2014, **90**, 214102.

38 S. Bhaskar, S. B. Majumder and R. S. Katiyar, *Appl. Phys. Lett.*, 2002, **80**, 3997–3999.

39 J. Chen, Y. Qi, G. Shi, X. Yan, S. Yu and J. Cheng, *J. Appl. Phys.*, 2008, **104**, 064124.

40 A. A. Bokov, L. A. Shpak and I. P. Rayevsky, *J. Phys. Chem. Solids*, 1993, **54**, 495–498.

41 G. Deng, G. Li, A. Ding and Q. Yin, *Appl. Phys. Lett.*, 2005, **87**, 192905.

42 W. Ji, X. He, W. Cheng, P. Qiu, X. Zeng, B. Xia and D. Wang, *Ceram. Int.*, 2015, **41**, 1950–1956.

43 L. Liu, D. Shi, Y. Huang, S. Wu, X. Chen, L. Fang and C. Hu, *Ferroelectrics*, 2012, **432**, 65–72.

44 J. T. S. Irvine, D. C. Sinclair and A. R. West, *Adv. Mater.*, 1990, **2**, 132–138.

45 S. Kumar and K. B. R. Varma, *Curr. Appl. Phys.*, 2011, **11**, 203–210.

46 J. F. Scott, *J. Phys.: Condens. Matter*, 2008, **20**, 021001.

47 A. K. Yadav, P. Rajput, O. Alshammari, M. Khan, V. Anita, G. Kumar, S. Kumar, P. M. Shirage, S. Biring and S. Sen, *J. Alloys Compd.*, 2017, **701**, 619–625.

48 J. P. Remeika and A. M. Glass, *Mater. Res. Bull.*, 1970, **5**, 37–45.

49 L. Yang, Y. Zhao, S. Zhang, P. Li, Y. Gao, Y. Yang, H. Huang, P. Miao, Y. Liu, A. Chen, C. W. Nan and C. Gao, *Sci. Rep.*, 2014, **4**, 4591.

50 S. Chopra, S. Sharma, T. C. Goel and R. G. Mendiratta, *Ferroelectrics*, 2005, **327**, 97–101.

51 R. Koduri and L. Marta, *J. Phys. D: Appl. Phys.*, 2006, **39**, 4466.

52 M. Prabu, I. B. Shameem Banu, S. Gobalakrishnan and M. Chavali, *J. Alloys Compd.*, 2013, **551**, 200–207.

53 H. Beltrán, E. Cordoncillo, P. Escribano, D. C. Sinclair and A. R. West, *J. Appl. Phys.*, 2005, **98**, 094102.

54 M. Li, J. Li, L.-Q. Chen, B.-L. Gu and W. Duan, *Phys. Rev. B: Condens. Matter Mater. Phys.*, 2015, **92**, 115435.

55 L. Liu, H. Fan, L. Fang, X. Chen, H. Dammak and M. P. Thi, *Mater. Chem. Phys.*, 2009, **117**, 138–141.

56 F. A. Kröger and H. J. Vink, *Solid State Phys.*, 1956, **3**, 307–435.

57 N. Yuji, M. Ichiro, G. Yu and M. Masaru, *Jpn. J. Appl. Phys., Part 2*, 2000, **39**, L1259.